



# Inter-clusters synergy in iron-organic frameworks for efficient CO<sub>2</sub> photoreduction

Yu-Jie Wang<sup>a,b</sup>, Hong-Juan Wang<sup>b</sup>, Fang Luo<sup>a,\*\*</sup>, Shuang Yao<sup>b</sup>, Tong-Bu Lu<sup>b</sup>, Zhi-Ming Zhang<sup>a,b,\*</sup>

<sup>a</sup> Key Laboratory of Polyoxometalate and Reticular Material Chemistry of Ministry of Education, Northeast Normal University, Changchun 130024, China

<sup>b</sup> Institute for New Energy Materials & Low Carbon Technologies, School of Materials Science & Engineering, Tianjin University of Technology, Tianjin 300384, China

## ARTICLE INFO

### Keywords:

Metal-organic framework  
Dual-nuclear cluster  
CO<sub>2</sub> photoreduction  
Inter-clusters synergy

## ABSTRACT

It is extremely desirable to explore molecular catalysts with precise structure for in-depth exploring structure-activity relationship of CO<sub>2</sub> photoreduction. Herein, we demonstrate the precise encapsulation of dual-nuclear clusters {Fe<sub>2</sub>(H<sub>2</sub>O)<sub>6</sub>(triazole)<sub>3</sub>} into metal-organic frameworks (MOFs) via ligand substitution strategy, resulting in two Fe<sub>2</sub>@Fe<sub>3</sub>-MOF composites (Fe<sub>3</sub>-Fe<sub>2</sub> and NH<sub>2</sub>-Fe<sub>3</sub>-Fe<sub>2</sub>). The fixed distance between two adjacent Fe<sub>3</sub>(μ<sub>3</sub>-O)Cl(H<sub>2</sub>O)<sub>2</sub> nodes in the MOF matrix allows the Fe<sub>2</sub>-Tri clusters to be fixed at a predetermined distance to unveil the critical role in improving the activity and selectivity for CO<sub>2</sub> reduction. The performance of Fe<sub>3</sub>-Fe<sub>2</sub> and NH<sub>2</sub>-Fe<sub>3</sub>-Fe<sub>2</sub> can reach to 309.3 and 395.5 μmol g<sup>-1</sup> h<sup>-1</sup> respectively, much superior to most of the state-of-the-art MOF catalysts. Such high activity and selectivity for formate generation can be attributed to the inter-clusters synergy mediated via in situ formed H-bonds and the cluster-framework cooperativity, supported by the results of DFT calculations and systemic experimental characterizations.

## 1. Introduction

Direct solar-driven CO<sub>2</sub> reduction into valuable chemicals (such as CH<sub>4</sub>, CO, CH<sub>3</sub>OH and HCOOH) represents a desirable approach to address the energy crisis and environmental pollution [1–3]. Among these valuable products, formic acid, as an important liquid chemical, has been widely used as preservative, important carbon source in industrial synthesis, and has potential applications in the fields of formic acid fuel cells and hydrogen storage [4,5]. For CO<sub>2</sub> photoreduction, ingenious design of catalysts is the key to improving catalytic performance and controlling the selectivity [6,7]. To date, numerous efforts have been devoted to exploring earth-abundant metal-complexes as highly selective catalysts, however most of them are synthesized for CO generation, only a few for formic acid liquid fuels [8]. Therefore, it is extremely desirable for exploring efficient molecular catalysts with well-defined structure to achieve highly selective formate generation with high activity.

Among the artificial photosynthesis, great progress has been

achieved in the construction of molecular catalysts for CO<sub>2</sub> reduction for in-depth understanding the catalytic process at molecular level, including the Fe, Co, Ni and Cu-based complexes [9–14]. In this field, these molecular catalysts were often used in the homogeneous catalytic systems, which make a serious difficulty for their recycling. Moreover, such systems often require a large amount of precious metal antenna molecules to sensitize molecular catalysts [15–18]. How to achieve heterogeneity of molecular catalysts and maintain their precise structure to construct inexpensive artificial photosynthesis systems is still a longstanding and extremely attractive task.

Biological systems are known to accomplish different substrate recognition and highly efficient transformation as the ubiquitous existence of multi-metallic cooperativity of metalloenzymes. Inspired by biological systems, considerable efforts have been devoted to the synthesis of multi-nuclear cluster catalysts for synergistic photocatalysis to achieve efficient and high selective artificial photosynthesis. In this field, we are interested in constructing dual-nuclear cluster to achieve bimetallic synergy for CO<sub>2</sub> photoreduction. In the case of Co-Co

\* Corresponding author at: Institute for New Energy Materials & Low Carbon Technologies, School of Materials Science & Engineering, Tianjin University of Technology, Tianjin 300384, China.

\*\* Corresponding author at: Key Laboratory of Polyoxometalate and Reticular Material Chemistry of Ministry of Education, Northeast Normal University, Changchun 130024, China.

E-mail addresses: [luof746@nenu.edu.cn](mailto:luof746@nenu.edu.cn) (F. Luo), [zmzhang@email.tjut.edu.cn](mailto:zmzhang@email.tjut.edu.cn) (Z.-M. Zhang).

<https://doi.org/10.1016/j.apcatb.2021.120487>

Received 15 April 2021; Received in revised form 7 June 2021; Accepted 23 June 2021

Available online 24 June 2021

0926-3373/© 2021 Published by Elsevier B.V.

cooperativity in a  $[\text{Co}_2(\text{OH})\text{L}_1]^{3+}$  molecular catalyst, it exhibits much higher performance (TON of 16896) and selectivity (CO 98%) than the corresponding mononuclear catalyst [19]. Replacing one  $\text{Co}^{2+}$  in this  $[\text{Co}_2(\text{OH})\text{L}_1]^{3+}$  complex by a  $\text{Zn}^{2+}$  can further dramatically boost CO evolution to give direct evidence of synergistic catalysis [20]. Recently, a mononuclear  $\text{Ni}^{2+}$  complex with pyridine dendants was used to capture  $\text{Mg}^{2+}$  to achieve bimetallic cooperativity for improving  $\text{CO}_2$  photoreduction into CO [21]. The synergistic catalysis effect was also observed in selectively electrocatalytic  $\text{CO}_2$  reduction to CO in a Fe-carbonyl cluster [22]. From above examples, it can be concluded that the atomic type, appropriate atomic distance and the special coordination environment in the multinuclear catalysts must be combined with the catalytic requirements to drive corresponding catalytic reaction. As a result, the cluster catalysts acting in synergy for  $\text{CO}_2$  reduction are very rare, which remains a major challenge for synthetic and catalytic chemistry. A recent example reports the selectivity control of CO versus  $\text{HCOO}^-$  production from  $\text{CO}_2$  photoreduction via riveting two mononuclear  $[\text{Co}(\text{qpy})]^{2+}$  active centers into dinuclear catalyst  $[\text{Co}_2\text{biqpy}]^{4+}$  with adjustable distance [23]. Its selectivity can be easily steered towards the desired product by simply changing the acid co-substrate. These results suggest that it should be an effective strategy for constructing synergistic catalytic systems by fixing existing active centers, including single-site and cluster catalysts, at an appropriate distance in a special matrix.

Metal organic frameworks (MOFs) are a family of porous crystalline materials with well-defined structure, their inherent large surface areas, easily tunable structures/components have enabled them a variety of potential applications [24–31]. Especially, they have been widely used as the versatile platforms to encapsulate multiple components to achieve efficient solar energy utilization [32–40]. Lin's group report the cooperative of  $\text{Cu}^{\text{I}}$  sites on a  $\text{Zr}_{12}$  cluster in a MOF matrix for selective  $\text{CO}_2$  hydrogenation to ethanol, which can be used for selectivity control of ethanol versus methanol production [36]. Jiang et al. installed  $\text{Fe}^{3+}$  cations onto the Zr-oxo clusters in a UiO-MOF to construct Fe-based MOF, which features extended visible light harvesting, based on metal-to-cluster charge transfer (MCCT) [38]. Lan et al. reported two polyoxometalate-metalloporphyrin coordination frameworks for highly selective  $\text{CH}_4$  formation (>96 %) [40]. The integration of photosensitizers and catalysts into one MOF matrix can successfully achieve their heterogeneity with much enhanced performance as two cooperative components. Therefore, photosensitizing MOFs represent a class of ideal platforms for fixing catalysts at a special distance to achieve both the inter-catalysts synergy and catalyst-framework cooperativity, however, never achieved for highly selective  $\text{CO}_2$  photoreduction to liquid product.

Herein, two  $\text{Fe}_3$ -MOFs  $\{\text{Fe}_3(\mu_3\text{-O})\text{Cl}(\text{H}_2\text{O})_2(\text{BDC})_3\}$  ( $\text{Fe}_3$ ) and  $\{\text{Fe}_3(\mu_3\text{-O})\text{Cl}(\text{H}_2\text{O})_2(\text{NH}_2\text{-BDC})_3\}$  ( $\text{NH}_2\text{-Fe}_3$ ) were used as the platforms to fix dual-nuclear  $\{\text{Fe}_2(\text{H}_2\text{O})_6(\text{triazole})_3\}$  ( $\text{Fe}_2\text{-Tri}$ ,  $\text{Tri}$  = triazole) clusters, resulting in the composites of  $\{[\text{Fe}_2\text{-Tri}]\{\text{Fe}_3(\mu_3\text{-O})(\text{BDC})_3\}\cdot 4\text{NO}_3\}$  ( $\text{Fe}_3\text{-Fe}_2$ ,  $\text{H}_2\text{BDC}$  = benzene-1,4 dicarboxylate acid) and  $\{[\text{Fe}_2\text{-Tri}]\{\text{Fe}_3(\mu_3\text{-O})(\text{NH}_2\text{-BDC})_3\}\cdot 4\text{NO}_3\}$  ( $\text{NH}_2\text{-Fe}_3\text{-Fe}_2$ ;  $\text{NH}_2\text{-H}_2\text{BDC}$  = 2-amino-benzene-1,4-dicarboxylate acid). The  $\text{Fe}_2\text{-Tri}$  clusters are precisely fixed in the MOF matrix via the ligand replacement. The fixed distance between two adjacent  $\text{Fe}_3(\mu_3\text{-O})$  nodes in the  $\text{Fe}_3$ -MOFs allows the  $\text{Fe}_2\text{-Tri}$  clusters to be fixed at a predetermined distance to unveil the critical role of the inter-clusters synergy for improving the activity and selectivity for  $\text{CO}_2$  reduction. As a result, the photocatalytic performance of  $\text{Fe}_3\text{-Fe}_2$  and  $\text{NH}_2\text{-Fe}_3\text{-Fe}_2$  can reach to as high as 309.3 and 395.5  $\mu\text{mol g}^{-1} \text{h}^{-1}$  with nearly 100% formate selectivity, in the absence of any noble-metal photosensitizers. This performance was much higher than that of isolated  $\text{Fe}_3$ -MOFs, and superior to most of the state-of-the-art MOF catalysts. Notably, the introduction of dual-nuclear clusters not only dramatically improves the catalytic efficiency of the MOFs, but also greatly enhances their chemical and photochemical stability.

## 2. Experimental section

### 2.1. Materials

All chemicals were commercially available and used without further purification. UV-vis diffuse reflectance spectra were taken using a UV-vis near-infrared spectrophotometer (Lambda 750 UV/VIS/NIR, PerkinElmer, America). Powder X-ray diffraction (PXRD) data were collected by a Smart X-ray diffractometer (SmartLab 9 KW, Rigaku, Japan) with Cu  $K\alpha$  radiation ( $\lambda = 1.54178 \text{ \AA}$ ). The photoluminescence (PL) spectra were conducted on a fluorescence spectrophotometer (F-7000, Hitachi, Japan). The amount of CO and  $\text{CH}_4$  generated in the photocatalytic process was quantified using gas chromatograph (GC-2014, Shimadzu, Japan). Cyclic voltammograms (CVs) were recorded on a CHI 760E electrochemical work station at room temperature. The  $\text{HCOOH}$  produced in the photocatalytic reaction was measured by Ion Chromatography (ECO IC, Metrohm, Switzerland) and NMR spectroscopy (ECZ400S, AVANCE III).

### 2.2. Synthesis

#### 2.2.1. Synthesis of $\text{Fe}_3$

$\text{Fe}_3$  and its  $\text{NH}_2$ -functionalized derivatives were synthesized according to the literature [47]. The  $\text{Fe}_3$  MOF was prepared via a hydrothermal treatment of  $\text{FeCl}_3\cdot 6\text{H}_2\text{O}$  and terephthalic acid ( $\text{H}_2\text{BDC}$ ) (1:1) in DMF at  $110^\circ\text{C}$  for 12 h. The crystals were soaked in 20 mL of acetonitrile for 3 days, filtered and dried under vacuum for further characterization.

#### 2.2.2. Synthesis of $\text{NH}_2\text{-Fe}_3$

$\text{NH}_2\text{-Fe}_3$  MOF was prepared via a hydrothermal treatment of  $\text{FeCl}_3\cdot 6\text{H}_2\text{O}$  and 2-aminoterephthalic acid ( $\text{NH}_2\text{-BDC}$ ) (1:1) in DMF at  $110^\circ\text{C}$  for 12 h. The crystals were soaked in 20 mL of acetonitrile for 3 days, filtered and dried under vacuum for further characterization [47].

#### 2.2.3. Synthesis of $\text{Fe}_3\text{-Fe}_2$

$\text{Fe}(\text{NO}_3)_3\cdot 9\text{H}_2\text{O}$  (80 mg, 0.2 mmol), terephthalic acid (33 mg, 0.2 mmol), 1,2,4-triazole (14 mg, 0.2 mmol) and L-tartaric acid (30 mg, 0.2 mmol) were added in the mixed solvent of DMF (2 mL)/glacial acetic acid (0.4 mL) in a 5 mL vial. The mixture was stirred for half an hour and heated at  $120^\circ\text{C}$  for 60 h, followed by cooling down to room temperature. Black block crystals were obtained. The crystals were soaked in 20 mL of water for 3 days, filtered and dried under vacuum for further characterization.

#### 2.2.4. Synthesis of $\text{NH}_2\text{-Fe}_3\text{-Fe}_2$

$\text{Fe}(\text{NO}_3)_3\cdot 9\text{H}_2\text{O}$  (80 mg, 0.2 mmol), 2-aminoterephthalic acid  $\text{NH}_2\text{-BDC}$  (36 mg, 0.2 mmol), 1,2,4-triazole (14 mg, 0.2 mmol) and L-tartaric acid (30 mg, 0.2 mmol) were added into the mixed solvent of DMF (2 mL)/glacial acetic acid (0.4 mL) in a 5 mL vial. The mixture was stirred for half an hour and heated at  $120^\circ\text{C}$  for 48 h, followed by cooling down to room temperature. Black block crystals were obtained. The crystals were soaked in 20 mL of water for 3 days, filtered and dried under vacuum for further characterization.

### 2.3. Photocatalytic experiments

The photocatalytic reduction of  $\text{CO}_2$  was carried out in a 17 mL reactor and irradiated under a 300-W Xe lamp. Prior to light illumination, the high-purity  $\text{CO}_2$  gas was bubbled into the reaction setup to reach a pressure of 1 atm. In a typical reaction system, the catalyst (2 mg) was suspended in 8 mL acetonitrile/ $\text{H}_2\text{O}$  ( $v/v = 1:1$ ) containing 0.1 mL triisopropanolamine (0.1 M), by stirring with a magnetic stirrer. The generated gas products were analyzed by gas chromatograph (GC-2014, Shimadzu, Japan). The filtrate of the reaction was measured by Ion Chromatography (Impact II Q-TOF) and NMR spectroscopy (ECZ400S, AVANCE III). Each reaction was repeated three times to ensure the

reliability of the experiment data. The  $^{13}\text{CO}_2$  labeling experiments were performed with a mixture of catalyst (5 mg) in 8 mL acetonitrile/ $\text{H}_2\text{O}$  (v/v = 1:1), containing 0.1 mL triisopropanolamine (0.1 M). The flask was then evacuated to ensure air removal and purged with Ar to the normal pressure followed by purging with  $^{13}\text{CO}_2$ .

## 2.4. Electrochemical measurements

An indium tin oxide (ITO) glass with  $1\text{ cm}^2$  deposition area was used as the support for the working electrode. The sample suspensions were prepared by dispersing 2 mg of catalyst catalyst in the solution containing 1 mL of ethanol and 10  $\mu\text{L}$  Nafion followed by ultrasonication for 60 min. Then, 40  $\mu\text{L}$  of the suspension was pipetted onto the ITO and dried at ambient temperature, which was used as the working electrode. The measurements were measured on an electrochemical analyzer (CHI760E) in a standard three-electrode cell, with working electrode (ITO), reference electrode Ag/AgCl (3M KCl) and counter electrode platinum plate. All the experiments were performed at room temperature in 0.2 M  $\text{Na}_2\text{SO}_4$  electrolyte (pH = 6.8). Mott-Schottky measurements were conducted at frequencies of 1000, 1500, 2000 Hz in the potential range. Photocurrent tests were performed at the potential of  $-0.87\text{ V}$  vs. Ag/AgCl excited by a 300 W Xe lamp.

## 3. Results and discussion

### 3.1. Synthesis and characterization

These  $\text{Fe}_3$  and  $\text{NH}_2\text{-Fe}_3$  MOFs are composed of  $\text{Fe}_3(\mu_3\text{-O})$  nodes fused together by terephthalic acid and  $\text{NH}_2\text{-BDC}$  linkers [41]. The  $\text{Fe}_3(\mu_3\text{-O})$  clusters were uniformly fixed in the MOF matrix, and the  $\text{Cl}^-$  and water molecules on their surface can be easily replaced by organic molecules [42], providing potential coordination sites for linker installation to further precisely embed catalytic active centers (Fig. 1). Here, we employed these  $\text{Fe}_3$  and  $\text{NH}_2\text{-Fe}_3$  MOFs as the carrier to realize the precise immobilization of dinuclear ferric clusters to construct the single crystal of  $\text{NH}_2\text{-Fe}_3\text{-Fe}_2$  and  $\text{Fe}_3\text{-Fe}_2$  molecular composites. Block crystals of  $\text{Fe}_3\text{-Fe}_2$  and  $\text{NH}_2\text{-Fe}_3\text{-Fe}_2$  MOFs were facilely prepared by a one-pot reaction of  $\text{Fe}(\text{NO}_3)_3$ , Tri and  $\text{NH}_2\text{-BDC/BDC}$  in  $N,N$ -dimethylformamide (DMF) (Fig. S1 and S2). The XRD pattern of the as-prepared  $\text{NH}_2\text{-Fe}_3\text{-Fe}_2$  product was similar to that of  $\text{Fe}_3\text{-Fe}_2$  (Fig. 2c), indicating a similar structure of  $\text{NH}_2\text{-Fe}_3\text{-Fe}_2$  and  $\text{Fe}_3\text{-Fe}_2$ . Single crystal X-ray diffraction analysis of  $\text{Fe}_3\text{-Fe}_2$  reveals that these crystals crystallize in the hexagonal  $\text{P6(3)/mmc}$  space group (Table S1). As shown in Fig. 1 and S3, the octahedral coordination environment of Fe1 center in the

$\text{Fe}_2\text{-Tri}$  cluster is completed by three N atoms from three Tri ligands and three water molecules (Fig. S3a). Moreover, two nearby Fe1 centers constitute a paddle-wheel unit fused together by three Tri linking units (Fig. S5). The Fe2 center in the  $\text{Fe}_3(\mu_3\text{-O})$  unit in the  $\text{Fe}_3\text{-Fe}_2$  MOFs also exhibits an octahedral coordination environment, which is constructed by four carboxylate O atoms, one  $\mu_3\text{-O}$  atom and one N atom from one Tri (Fig. S3b). Each Tri ligand further links to two Fe1 centers to fix the  $\text{Fe}_2\text{-Tri}$  cluster. The arrangement of its open metal sites in the MOF matrix perfectly fits the size and geometry of triangular tridentate metalloligands consisting three Tri ligands with a dual-nuclear cluster, giving structurally reinforced on these  $\text{Fe}_3\text{-MOFs}$  (Fig. S4–S8). The paddle-wheel-like dual-nuclear cluster consists of two Fe centers and three Tri ligands, and each Fe center coordinates with three oxygen atoms from terminal water molecules (Fig. 1b and S5). The paddle-wheel-like  $\text{Fe}_2\text{-Tri}$  clusters were fixed into the  $\text{Fe}_3\text{-MOF}$  matrix via the Tri ligands by replacing coordinated water molecules in the  $\text{Fe}_3(\mu_3\text{-O})$  cluster (Fig. 1b). It is worth noting that the separation of  $\text{Fe}\cdots\text{Fe}$  in two adjacent  $\text{Fe}_2\text{-Tri}$  clusters is only 0.513 nm with the  $\text{H}_2\text{O}\cdots\text{H}_2\text{O}$  distance of 0.309 nm, which may facilitate synergistic catalysis between two dual-nuclear clusters. The TEM characterization was further performed on these samples, where the large MOF particles are crushed by ball mill. From the TEM and EDX elemental mapping images, it can be observed that the C, N, O and Fe elements exist in the MOF crystals (Fig. S9).

In addition, X-ray photoelectron spectroscopy (XPS) was performed to reveal the surface chemical composition and the valence state of the metal ions. In the XPS spectroscopy, the Fe  $2p_{3/2}$  and  $2p_{1/2}$  peaks located at 712.5 and 725.3 eV indicate the +3 oxidation state of Fe centers in both the  $\text{Fe}_3\text{-Fe}_2$  and  $\text{NH}_2\text{-Fe}_3\text{-Fe}_2$  MOFs (Fig. S10). The phase purity of  $\text{NH}_2\text{-Fe}_3\text{-Fe}_2$  and  $\text{Fe}_3\text{-Fe}_2$  was confirmed by power X-ray diffraction (XRD) and the fourier transform infrared (FTIR) spectroscopy. The XRD pattern of the as-prepared products was similar to that simulated from the single-crystal X-ray diffraction data (Fig. 2c), indicating they have a similar structure with high phase purity. In the FTIR spectra, the absorption peaks at  $1602\text{ cm}^{-1}$ ,  $1288\text{ cm}^{-1}$  for  $\text{Fe}_3\text{-Fe}_2$  and  $\text{NH}_2\text{-Fe}_3\text{-Fe}_2$  can be attributed to the Tri groups (Fig. S11), confirming the introduction of  $\text{Fe}_2\text{-Tri}$  in the MOF matrix. Chemical stability of these MOFs was carefully studied. It can be observed that the isolated  $\text{Fe}_3\text{-MOFs}$  collapsed instantly when they were dispersed into the water (Fig. S12). As shown in Fig. S13, the  $\text{NH}_2\text{-Fe}_3\text{-Fe}_2$  and  $\text{Fe}_3\text{-Fe}_2$  MOFs can maintain their structure in various solution with the pH range of 1–13 for 24 h. The thermal gravimetric analysis (TGA) was further performed to study the thermal stability these Fe-MOFs. As shown in Fig. S14, the TGA curve of as-synthesized  $\text{Fe}_3\text{-Fe}_2\text{-MOFs}$  was measured from room

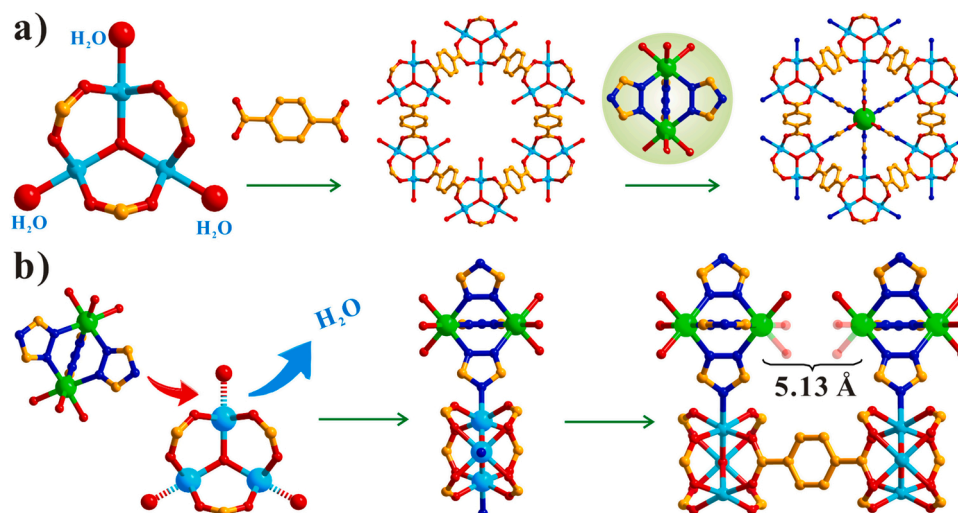
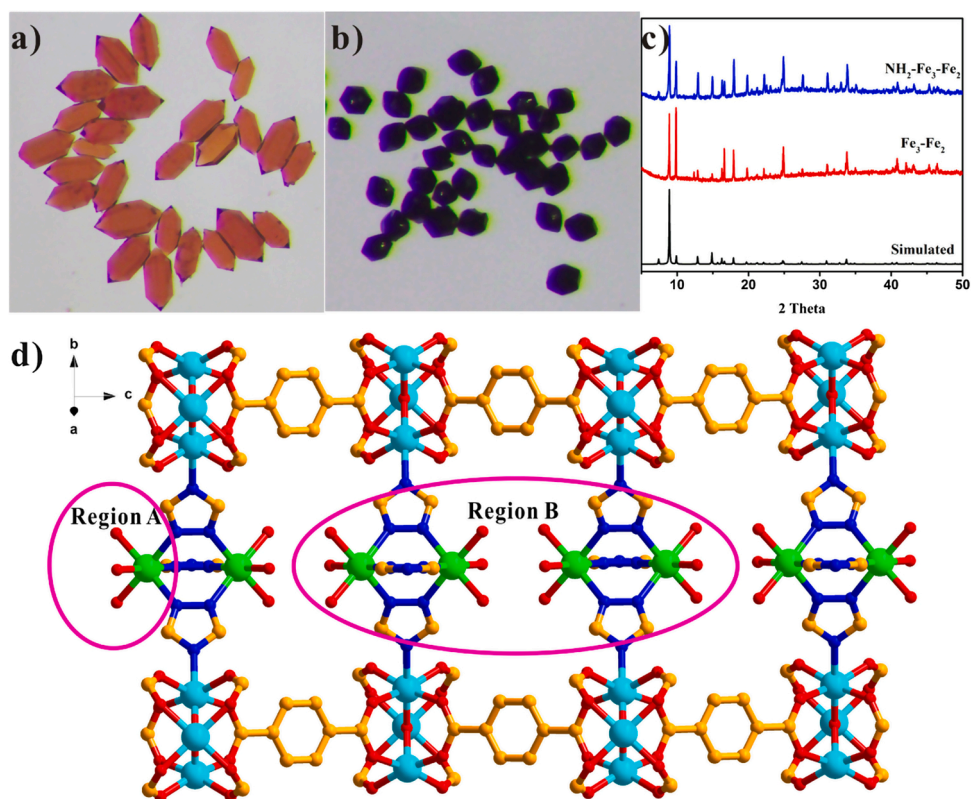
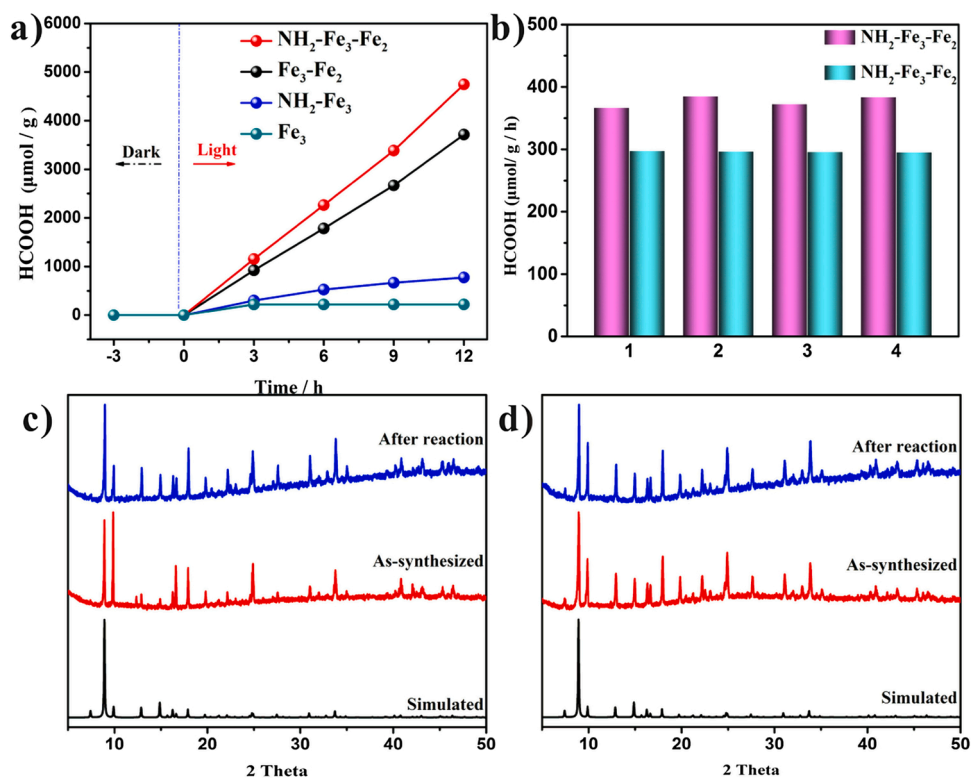


Fig. 1. a) Assembly  $\text{Fe}_3\text{-Fe}_2$  MOFs. b) Fixation of  $\text{Fe}_2\text{-Tri}$  on the surface of  $\text{Fe}_3(\mu_3\text{-O})$  cluster.



**Fig. 2.** Optical photographs of a) Fe<sub>3</sub> and b) Fe<sub>3</sub>-Fe<sub>2</sub>. PXRD patterns of c) Fe<sub>3</sub>-Fe<sub>2</sub> and NH<sub>2</sub>-Fe<sub>3</sub>-Fe<sub>2</sub> in comparison to the simulated PXRD pattern, d) the active sites exposed on the surface of the framework.



**Fig. 3.** a) Amounts of HCOOH produced as a function of the time of visible light irradiation. b) Recycle photocatalytic experiments. Experimental and simulated PXRD patterns of c) Fe<sub>3</sub>-Fe<sub>2</sub> and d) NH<sub>2</sub>-Fe<sub>3</sub>-Fe<sub>2</sub>.



temperature to 800 °C under N<sub>2</sub> atmosphere. The NH<sub>2</sub>-Fe<sub>3</sub>-Fe<sub>2</sub> and Fe<sub>3</sub>-Fe<sub>2</sub> MOFs show a similar TGA behavior. For NH<sub>2</sub>-Fe<sub>3</sub>-Fe<sub>2</sub>, two continuous weight losses (32.6%) from room temperature to 323 °C corresponds to the release four NO<sub>3</sub><sup>−</sup> (calcd. 17.9%), six coordinated water molecules (calcd. 7.7 %). For Fe<sub>3</sub>-Fe<sub>2</sub>, a similar TGA behavior can be observed, where the two continuous weight losses (32.8%) correspond to the release of four NO<sub>3</sub><sup>−</sup> (calcd. 18.7%) and six coordinated water molecules (calcd. 8.0 %). It can be observed that the first two continuous weight losses (32.6% for NH<sub>2</sub>-Fe<sub>3</sub>-Fe<sub>2</sub>, 32.8% for Fe<sub>3</sub>-Fe<sub>2</sub>) was higher than that for the calcd. losses of 25.6 % (NH<sub>2</sub>-Fe<sub>3</sub>-Fe<sub>2</sub>) and 26.7% (Fe<sub>3</sub>-Fe<sub>2</sub>), indicating the existence of some solvent molecules in the pore the MOFs. Before the photocatalysis, these solvent molecules have been removed, as a result, it cannot influence the photocatalytic results. Further, the NH<sub>2</sub>-Fe<sub>3</sub>-Fe<sub>2</sub> and Fe<sub>3</sub>-Fe<sub>2</sub> MOFs can still maintain their framework structure up to 450 °C. On further increasing the heating temperature, the weight loss was assigned to the release of Tri and BDC/NH<sub>2</sub>-BDC ligands. These results showed that NH<sub>2</sub>-Fe<sub>3</sub>-Fe<sub>2</sub> and Fe<sub>3</sub>-Fe<sub>2</sub> possess of excellent thermal stability. Notably, their robustness can also be maintained under traditional photocatalytic condition for CO<sub>2</sub> reduction (Fig. 3c and d). All these results demonstrate that the chemical and photochemical stability can be both dramatically improved after the introduction of dual-nuclear clusters.

As shown in Fig. 2a and b, the fusiform orange-yellow crystals became to black polyhedral crystals after loading the Fe<sub>2</sub>-Tri clusters, and in the UV-vis spectra, the NH<sub>2</sub>-Fe<sub>3</sub>-Fe<sub>2</sub> and Fe<sub>3</sub>-Fe<sub>2</sub> exhibits a broad-band visible light absorption (Fig. S15a), indicating the changes in their optical properties. For a detail comparison of optical properties and the MOF structures (Fig. S16), it can be found that the introduction of Fe<sub>2</sub>-Tri cluster plays an important role in improving the optical absorption of NH<sub>2</sub>-Fe<sub>3</sub>-Fe<sub>2</sub> and Fe<sub>3</sub>-Fe<sub>2</sub>. Further, NH<sub>2</sub>-Fe<sub>3</sub>-Fe<sub>2</sub> shows a more broaden visible light

absorption compared to that of Fe<sub>3</sub>-Fe<sub>2</sub>. These results demonstrated that the modification of the linkers and clusters was beneficial for broadening the light-harvesting [43–46]. For NH<sub>2</sub>-Fe<sub>3</sub>-Fe<sub>2</sub> and Fe<sub>3</sub>-Fe<sub>2</sub>, the electron transfer from the organic linker to Fe<sub>3</sub>(μ<sub>3</sub>-O) and Fe<sub>2</sub>-Tri clusters was studied by photoluminescence (PL) spectra. As displayed in Fig. S17, when excited at 370 nm, BDC and NH<sub>2</sub>-BDC showed a broad luminescence band centered at 435 nm and 550 nm respectively, which can be attributed to its local excitation. However, NH<sub>2</sub>-Fe<sub>3</sub>-Fe<sub>2</sub> and Fe<sub>3</sub>-Fe<sub>2</sub> did not show any PL signal around 435 nm and 550 nm, suggesting the efficient energy transfer from excited BDC and BDC-NH<sub>2</sub> organic linker to metal clusters. To further elucidate the charge transfer process, photocurrent measurements were employed to reveal the separation efficiency of photogenerated carrier. The I-t curves with visible-light illumination show that NH<sub>2</sub>-Fe<sub>3</sub>-Fe<sub>2</sub> possesses the highest photocurrent among these Fe-based MOFs, suggesting the most efficient intrinsic electron transfer in the NH<sub>2</sub>-Fe<sub>3</sub>-Fe<sub>2</sub> composite (Fig. S18). The charge transfer between the organic linkers and the iron center was further studied by synchronous illumination XPS. Under light irradiation, both Fe 2p<sub>3/2</sub> and Fe 2p<sub>1/2</sub> peaks shifted to a lower binding energy in reference to that of pristine MOF (Fig. S19), indicating charge excitation and transfer from ligands to the iron species.

To elucidate the band structures of NH<sub>2</sub>-Fe<sub>3</sub>-Fe<sub>2</sub> and Fe<sub>3</sub>-Fe<sub>2</sub> and their possibility for subsequent CO<sub>2</sub> photoreduction, Mott-Schottky measurements were conducted at frequencies of 1000, 1500, and 2000 Hz. As shown in Fig. S15 and S16, the LUMO locations of Fe<sub>3</sub>-Fe<sub>2</sub> and NH<sub>2</sub>-Fe<sub>3</sub>-Fe<sub>2</sub> were determined to be −1.11 and −1.18 eV versus NHE. These LUMO locations are more negative than the reduction potentials for CO<sub>2</sub> photoreduction to many products, such as HCOOH (−0.61 V vs. NHE) and CO (−0.53 V vs. NHE), indicating that the photo-generated electrons can migrate to CO<sub>2</sub> molecule to drive the reduction reactions. Their band gaps were calculated to be 2.53 (Fe<sub>3</sub>-Fe<sub>2</sub>) and 2.45 eV (NH<sub>2</sub>-Fe<sub>3</sub>-Fe<sub>2</sub>) by the Kubelka-Munk (KM) method, indicating their better light-harvesting ability to potentially act as efficient photocatalysts (Fig. S16). The LUMO location of NH<sub>2</sub>-Fe<sub>3</sub>-Fe<sub>2</sub> is very similar to that of Fe<sub>3</sub>-Fe<sub>2</sub>, demonstrating that the decoration of amine group in the

MOF framework has no obvious effect on the LUMO location. In order to prove this point, the LUMO of Fe<sub>3</sub> and NH<sub>2</sub>-Fe<sub>3</sub> was further determined, and the similar results can be obtained with the values of −0.95 and −0.96 eV for Fe<sub>3</sub> and NH<sub>2</sub>-Fe<sub>3</sub>, respectively.

### 3.2. CO<sub>2</sub> photoreduction and photochemical stability

The activity of CO<sub>2</sub> photoreduction of these Fe-MOFs was studied under visible light irradiation in CH<sub>3</sub>CN/H<sub>2</sub>O mixed solvent without additional photosensitizer. In the photocatalytic process, HCOOH was detected as the main product by ion chromatography (IC). On visible light irradiation, the yields of generated HCOOH increase steadily to 309.3 and 395.5 μmol g<sup>−1</sup> h<sup>−1</sup> for Fe<sub>3</sub>-Fe<sub>2</sub> and NH<sub>2</sub>-Fe<sub>3</sub>-Fe<sub>2</sub> with the irradiation time in 12 h, ca. 4 times higher than that of Fe<sub>3</sub> and NH<sub>2</sub>-Fe<sub>3</sub> under similar conditions, and superior to most of the state-of-the-art MOF catalysts (Table S2). No other gaseous and liquid products can be detected by gas chromatography (GC) in the photocatalytic process, suggesting an extremely high selectivity for CO<sub>2</sub>-to-HCOOH conversion. The reactor was scaled up to a 67 mL home-made quartz vessel instead of the previous 17-mL vial with the addition of five times of reagents, including 40 mL CH<sub>3</sub>CN/H<sub>2</sub>O (v:v = 1:1) saturated by CO<sub>2</sub>, NH<sub>2</sub>-Fe<sub>3</sub>-Fe<sub>2</sub> catalyst (25 mg), 0.5 mL TIPA (0.1 M). As shown in Fig. S20, the HCOO<sup>−</sup> yield can reach to 95.6 μmol and 382.4 μmol g<sup>−1</sup> h<sup>−1</sup> with ca. 100% selectivity with 10 h irradiation. This HCOO<sup>−</sup> production rate was similar to that obtained with 2 mg catalyst (Fig. S20). And the apparent quantum efficiency (AQE) is determined to be 0.023 %. A series of control experiments were carried out, such as in the absence of catalyst, light irradiation, triisopropanolamine (TIPA) or replacing CO<sub>2</sub> with Ar, the target product is undetectable (Fig. S21–S23). All these control experiments demonstrated the important role of catalyst for CO<sub>2</sub> photoreduction and eliminated the origin of HCOO<sup>−</sup> from the dissociation of the organic linkers, organic solvent and TIPA. To further verify the source of the obtained HCOO<sup>−</sup>, isotopic labeling experiment was performed by using <sup>13</sup>CO<sub>2</sub> as the carbon source (Fig. S24 and S25). The product was identified by <sup>13</sup>C NMR spectroscopy, and a peak at 164.8 ppm was detected and assigned to H<sup>13</sup>COO<sup>−</sup> (Fig. S24) [28]. To confirm the hydrogen source in the product of HCOOH, the CO<sub>2</sub> photoreduction was carried out in 4 mL anhydrous CH<sub>3</sub>CN, containing 0.1 mL TIPA (0.1 M), the HCOOH yield was only 49.7 μmol g<sup>−1</sup> h<sup>−1</sup>. When some H<sub>2</sub>O was added into the reaction system, the HCOOH yield can reach to 395.5 μmol g<sup>−1</sup> h<sup>−1</sup>, much enhanced compared to that in anhydrous CH<sub>3</sub>CN. Therefore, it can be preliminarily concluded that H<sub>2</sub>O is the hydrogen source of HCOOH. On the other hand, residual trace amount of water in anhydrous CH<sub>3</sub>CN should afford the HCOOH yield of 49.7 μmol g<sup>−1</sup> h<sup>−1</sup> (Fig. S26). These results unambiguously confirm that the produced HCOO<sup>−</sup> indeed comes from CO<sub>2</sub> photoreduction rather than the possible decomposition of organic components in the catalytic system. Recycle experiments were further performed to demonstrate the stability of the MOF catalysts. It could be found that no noticeable change in the HCOO<sup>−</sup> yield occurs during four recycle experiments (Fig. 3b). The XRD profile of Fe<sub>3</sub>-Fe<sub>2</sub> and NH<sub>2</sub>-Fe<sub>3</sub>-Fe<sub>2</sub> is retained after reaction (Fig. 3c and 3d). However, the Fe<sub>3</sub> and NH<sub>2</sub>-Fe<sub>3</sub> MOFs all lose their structural stability under the photocatalytic conditions. All these results indicate that the introduction of dual-nuclear clusters not only dramatically improve the catalytic efficiency of the MOFs, but also greatly enhance their photochemical stability.

### 3.3. Photocatalytic mechanism and DFT calculations

Generally, numerous factors can influence the catalytic activity of the framework materials, such as component, surrounding microenvironment of metal center, the structure of framework and pore characteristic. It is very difficult to explore the catalytic mechanism as the absence of the model system. Herein, to further highlight the important role of the dual-nuclear clusters in improving the catalytic performance, two pairs of frameworks of NH<sub>2</sub>-Fe<sub>3</sub>-Fe<sub>2</sub>/NH<sub>2</sub>-Fe<sub>3</sub> and Fe<sub>3</sub>-Fe<sub>2</sub>/Fe<sub>3</sub> with

similar structure are both designed and synthesized with only the difference at the  $\text{Fe}_2$ -Tri clusters. As shown in Fig. 3a, the evolution rate of HCOOH for  $\text{NH}_2\text{-Fe}_3\text{-Fe}_2$  and  $\text{Fe}_3\text{-Fe}_2$  was much enhanced compared to that of the isolated MOFs, which clearly demonstrates that the high activity of  $\text{NH}_2\text{-Fe}_2\text{-Fe}_3$  and  $\text{Fe}_2\text{-Fe}_3$  MOFs indeed derived from the presence of dual-nuclear  $\text{Fe}_2$ -Tri clusters in the well-defined crystalline frameworks. As shown in Fig. S27 and S28,  $\text{N}_2$  adsorption-desorption isotherms were measured at 77 K, and show typical type-I isotherms. The  $\text{NH}_2\text{-Fe}_3$  has a saturation uptake of  $122.3 \text{ cm}^3 (\text{STP}) \text{ g}^{-1}$ , which is much larger than that of  $\text{NH}_2\text{-Fe}_3\text{-Fe}_2$  ( $70.9 \text{ cm}^3 (\text{STP}) \text{ g}^{-1}$ ). These two MOFs possess Brunauer–Emmett–Teller (BET) specific surface areas of  $402.3 (\text{NH}_2\text{-Fe}_3)$  and  $233.6 (\text{NH}_2\text{-Fe}_3\text{-Fe}_2)$ , respectively. This observation reveals that the  $\text{Fe}_2$ -Tri clusters were successfully introduced into the pores of  $\text{NH}_2\text{-Fe}_3$ . Further,  $\text{CO}_2$  uptake experiments were performed with these two MOFs. Although the pores of  $\text{Fe}_3\text{-Fe}_2$  and  $\text{NH}_2\text{-Fe}_3\text{-Fe}_2$  are occupied by  $\text{Fe}_2$ -Tri clusters, and their density is larger than that of the  $\text{Fe}_3$  and  $\text{NH}_2\text{-Fe}_3$  MOFs, the  $\text{CO}_2$  uptake amount of  $\text{Fe}_3\text{-Fe}_2$  and  $\text{NH}_2\text{-Fe}_3\text{-Fe}_2$  is much higher than that of the isolated Fe-MOFs under the same condition (Fig. S29), indicating an important role of the  $\text{Fe}_2$ -Tri clusters in  $\text{CO}_2$  adsorption. Accordingly, it can be concluded that  $\text{CO}_2$  favorably binds to the  $\text{Fe}_2$ -Tri cluster, thus benefiting its conversion under visible-light irradiation.

Photoluminescence (PL) spectra were performed to reveal the separation efficiency of photoexcited electron-hole pairs. As shown in Fig. S30 and S31, the luminescence of BDC and  $\text{NH}_2\text{-BDC}$  can be efficiently quenched by  $\text{Fe}^{3+}$ , the quenching rate was much higher than that with the sacrificial agent TIPA as the quencher (Fig. S32–S34). These results indicated the electron transfer from the BDC (or  $\text{N}_2\text{H-BDC}$ ) to the  $\text{Fe}^{3+}$  center. Afterward, the TIPA was used to consume the photoinduced hole on the BDC, indicating an oxidation quenching mechanism in this photocatalytic process. All the above results demonstrate the TIPA and catalytic center  $\text{Fe}^{3+}$  all play an important role in the electron transfer process (Fig. S30–S34).

In the  $\text{Fe}_2$ -Tri cluster, it is worth noting that each Fe center was coordinated with three terminal water molecules in a pyramidal mode, which can be easily replaced by small substrate molecules during the catalytic process [14,20]. When  $\text{Fe}_2$ -Tri clusters are properly arranged in the MOF matrix, the separation of  $\text{Fe}\cdots\text{Fe}$  in two adjacent  $\text{Fe}_2$ -Tri clusters is only  $0.513 \text{ nm}$  with the  $\text{H}_2\text{O}\cdots\text{H}_2\text{O}$  distance of  $0.309 \text{ nm}$  (Fig. 4a). When  $\text{CO}_2$  molecule replaces one water molecule on the external site of one  $\text{Fe}_2$ -Tri cluster, some interaction with adjacent  $\text{Fe}_2$ -Tri cluster should occur during the  $\text{CO}_2$  capture. For this gas-solid-liquid reaction, even if the reaction occurs primarily on the surface of the catalyst, two adjacent  $\text{Fe}_2$ -Tri clusters in the region B can be exposed head-to-head on the surface of the framework for inter-cluster synergy (Fig. 2d). This may contribute greatly to the high activity and selectivity for  $\text{CO}_2$

photoreduction to formic acid. To further confirm this proposal, the photocatalytic activity of isolated  $\text{NH}_2\text{-Fe}_3$  MOF without  $\text{Fe}_2$ -Tri unit and  $\text{NH}_2\text{-MIL-101(Fe)}$  both composed of  $\text{Fe}_3(\mu_3\text{-O})$  cluster was evaluated, and their performance was much lower than that of  $\text{NH}_2\text{-Fe}_3\text{-Fe}_2$ , indicating that the  $\text{Fe}_2$ -Tri unit is more active than the  $\text{Fe}_3(\mu_3\text{-O})$  node in this framework (Fig. S35). In the  $\text{NH}_2\text{-Fe}_3\text{-Fe}_2$  MOF, the  $\text{Fe}_2$ -Tri cluster was fixed into the framework via replacing the  $\text{H}_2\text{O}$  molecule on the  $\text{Fe}_3(\mu_3\text{-O})$  node in the  $\text{NH}_2\text{-Fe}_3$  MOF. As a result, the Tri-functionalized  $\text{NH}_2\text{-Fe}_3$  MOF with the coordination unsaturated site occupied by Tri ligand can contribute very little to HCOOH yield in the  $\text{CO}_2$  photoreduction. Accordingly, the mass activity of Fe in  $\text{Fe}_2$ -Tri ( $4680.7 \mu\text{mol g}^{-1} \text{ h}^{-1}$ ) was much higher than that in  $\text{NH}_2\text{-MIL-101}$  ( $979.9 \mu\text{mol g}^{-1} \text{ h}^{-1}$ ). This extremely high activity of  $\text{Fe}_2$ -Tri implies a possible synergy between two adjacent clusters. This may contribute greatly to the high activity and selectivity for  $\text{CO}_2$  photoreduction to formic acid.

To confirm this proposal, DFT calculations were carried out to identify the active sites and deeply understand the mechanism of photocatalytic  $\text{CO}_2$  reduction at a molecular level. DFT calculations proposed a reasonable reaction pathway with four elementary steps for the reduction of  $\text{CO}_2$  to HCOOH. Firstly, the  $\text{CO}_2$  molecule was fixed on the catalytic active site by replacing one coordinated water molecule following the addition of one proton-electron pair to form an intermediate of  $^*\text{HCOO}$ . Then, the second proton-electron pair transferred to the  $^*\text{HCOO}$ , generating the  $^*\text{HCOOH}$ , and the finally, the adsorbed  $^*\text{HCOOH}$  molecule released from the active site to complete the catalytic cycle. During the simulation, one water molecule was removed to expose an unsaturated active site for the adsorption of  $\text{CO}_2$ , the isolated  $\text{Fe}_3(\mu_3\text{-O})(\text{H}_2\text{O})_3$ , isolated  $\text{Fe}_2$ -Tri cluster and inter-clusters synergy between two  $\text{Fe}_2$ -Tri clusters were selected as the models to perform this simulation (Fig. 5 and S36). The calculated free energy changes of the reaction pathways for three models were shown in Fig. 4b. For replacing one  $\text{H}_2\text{O}$  on the  $\text{Fe}_3(\mu_3\text{-O})$  cluster (Fig. S20), the initial adsorption and activation of  $\text{CO}_2$  molecule is endothermic, with a free energy change of  $1.097 \text{ eV}$ , indicating a weak interaction between the catalyst and the  $\text{CO}_2$  molecule. Then, the  $^*\text{HCOO}$  intermediate undergoes exothermic processes for the second hydrogenation and HCOOH desorption with the free energy changes of  $-0.651$  and  $-0.045 \text{ eV}$ , respectively. The free energy change for the formation of  $^*\text{HCOO}$  intermediate is much higher than that of the second proton-electron pair transfer and HCOOH desorption, indicating that the formation of  $^*\text{HCOO}$  intermediate is the rate-determining step for this model. On the other hand, the initial adsorption and activation of  $\text{CO}_2$  molecule on one  $\text{Fe}_2$ -Tri cluster (denoted as the  $\text{Fe}_2$ -Tri model) and between two  $\text{Fe}_2$ -Tri clusters (denoted as the  $\text{Fe}_3\text{-Fe}_2$  model) is an exothermic process, with the free energy change of  $-0.869$  and  $-1.206 \text{ eV}$ , showing a strong interaction between the catalyst and the adsorbate, in consistent with the  $\text{CO}_2$

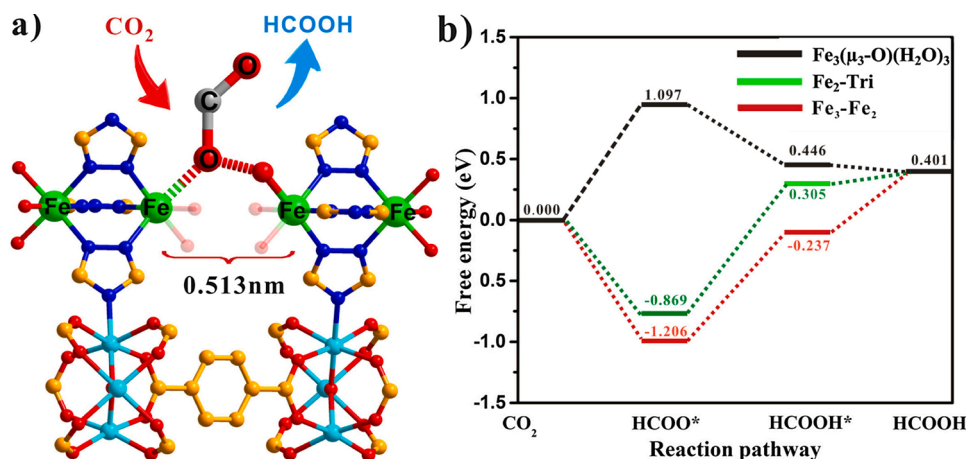
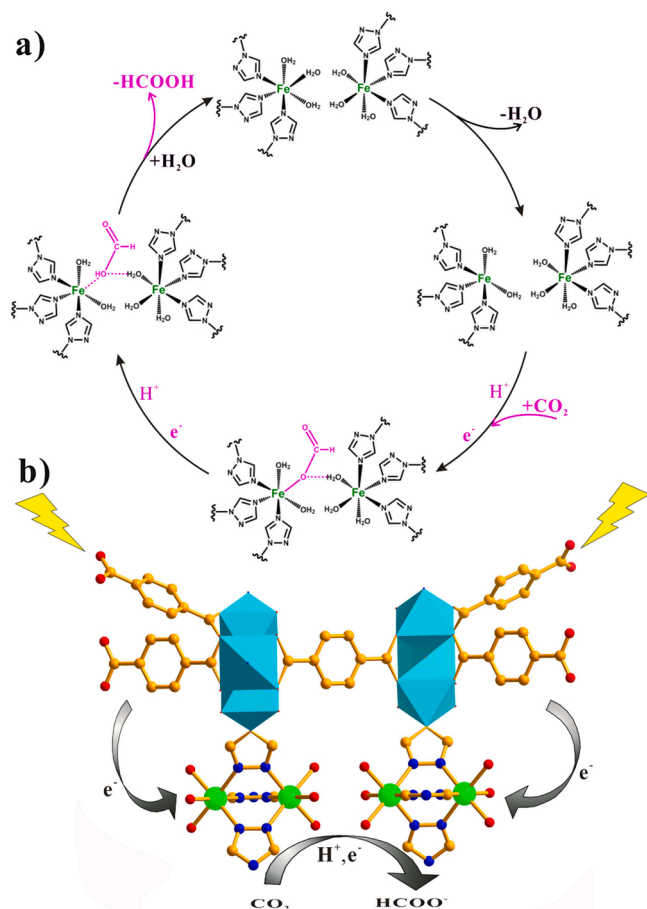


Fig. 4. a) Inter-clusters synergy between  $\text{Fe}_2$ -Tri clusters for  $\text{CO}_2$  reduction. b) Calculated free-energy diagram for  $\text{CO}_2$  photoreduction.



**Fig. 5.** a) Proposed CO<sub>2</sub>-to-HCOOH conversion pathway over Fe<sub>3</sub>-Fe<sub>2</sub> MOFs under visible light irradiation. b) Schematic show photocatalytic CO<sub>2</sub> reduction reaction by Fe-MOFs.

absorption results, probably due to the formation of hydrogen bonds between the \*HCOO intermediate and the adjacent coordination water molecules. The hydrogen bonds between the intermediates and water molecule were shown in Fig. 4a and S36. The formation of hydrogen bond with the water molecule in the same one Fe<sub>2</sub>-Tri cluster and in the adjacent Fe<sub>2</sub>-Tri cluster was both calculated. The hydrogen bonds were weakened along the second hydrogenation, making the rate-determining step for the Fe<sub>2</sub>-Tri and Fe<sub>3</sub>-Fe<sub>2</sub> with a free energy change of 1.174 and 0.969 eV, respectively. Due to the presence of the hydrogen bond, the HCOOH desorption for Fe<sub>2</sub> and Fe<sub>3</sub>-Fe<sub>2</sub> is endothermic, with a free energy change of 0.096 and 0.638 eV. It can be concluded that the inter-clusters synergy mediated via the in situ formed H-bonds between two adjacent clusters is beneficial for the conversion of the CO<sub>2</sub>-to-HCOOH and plays a vital role for the CO<sub>2</sub> activation.

#### 4. Conclusions

In summary, the dinuclear Fe<sub>2</sub>-Tri clusters were precisely embedded in a porous MOF matrix, resulting in two well-defined iron-based MOFs (NH<sub>2</sub>-Fe<sub>3</sub>-Fe<sub>2</sub> and Fe<sub>3</sub>-Fe<sub>2</sub>). The introduction of the dinuclear clusters into MOFs not only greatly improves the catalytic activity of these composite catalysts, but also dramatically enhances their chemical and photochemical stability. The resulting composites can act as highly efficient photocatalyst for CO<sub>2</sub> reduction with a nearly 100 % formate selectivity. This formate evolution rate of Fe<sub>3</sub>-Fe<sub>2</sub> and NH<sub>2</sub>-Fe<sub>3</sub>-Fe<sub>2</sub> can reach to as high as 309.3 and 395.5 μmol g<sup>-1</sup> h<sup>-1</sup> respectively in the absence of any noble-metal photosensitizers, much higher than that of isolated Fe<sub>3</sub>-MOFs, and superior to most of the state-of-the-art MOF

catalysts. Such high activity and selectivity for formate generation can be attributed to the inter-clusters synergy mediated via the in situ formed H-bonds and the cluster-framework cooperativity, supported by a combination of DFT calculations and various control experiments. These findings highlight a new strategy to design and synthesize new photocatalysts with synergistic catalysis effect for CO<sub>2</sub> photoreduction into liquid products in the artificial photosynthesis.

#### CRediT authorship contribution statement

**Yu-Jie Wang:** Conceptualization, Methodology, Data curation, Formal analysis, Writing - original draft. **Hong-Juan Wang:** DFT calculation. **Fang Luo:** Data curation. Supervision. **Shuang Yao:** Conceptualization, Formal analysis, Resources. **Zhi-Ming Zhang:** Conceptualization, Project administration, Formal analysis, Funding acquisition, Project administration, Writing - review & editing. **Tong-Bu Lu:** Supervision, Writing - review & editing.

#### Declaration of Competing Interest

The authors declare that they have no known competing financial interests or personal relationships that could have appeared to influence the work reported in this paper.

#### Acknowledgments

This work was supported by the National Natural Science Foundation of China (21971190, 22071180 and 21931007), Natural Science Foundation of Tianjin City of China (18JCJQJC47700).

#### Appendix A. Supplementary data

Supplementary material related to this article can be found, in the online version, at doi:<https://doi.org/10.1016/j.apcatb.2021.120487>.

#### References

- [1] Z. Jiang, X. Xu, Y. Ma, H.S. Cho, D. Ding, C. Wang, J. Wu, P. Oleynikov, M. Jia, J. Cheng, Y. Zhou, O. Terasaki, T. Peng, L. Zan, H.X. Deng, Filling metal-organic framework mesopores with TiO<sub>2</sub> for CO<sub>2</sub> photoreduction, *Nature* 586 (2020) 549–554, <https://doi.org/10.1038/s41586-020-2738-2>.
- [2] T. Kong, Y. Jiang, Y.J. Xiong, Photocatalytic CO<sub>2</sub> conversion: what can we learn from conventional CO<sub>x</sub> hydrogenation? *Chem. Soc. Rev.* 49 (2020) 6579–6591, <https://doi.org/10.1039/c9cs00920e>.
- [3] H.L. Zheng, S.L. Huang, M.B. Luo, Q. Wei, E.X. Chen, L. He, Q. Lin, Photochemical in situ exfoliation of metal-organic frameworks for enhanced visible-light-driven CO<sub>2</sub> reduction, *Angew. Chem. Int. Ed.* 59 (2020) 23588–23592, <https://doi.org/10.1002/anie.202012019>.
- [4] H. Rao, L.C. Schmidt, J. Bonin, M. Robert, Visible-light-driven methane formation from CO<sub>2</sub> with a molecular iron catalyst, *Nature* 548 (2017) 74–77, <https://doi.org/10.1038/nature23016>.
- [5] D.J. Boston, C. Xu, D.W. Armstrong, F.M. MacDonnell, Photochemical reduction of carbon dioxide to methanol and formate in a homogeneous system with pyridinium catalysts, *J. Am. Chem. Soc.* 135 (2013) 16252–16255, <https://doi.org/10.1021/ja406074w>.
- [6] B. Han, X. Ou, Z. Deng, Y. Song, C. Tian, H. Deng, Y.J. Xu, Z. Lin, Nickel metal-organic framework monolayers for photoreduction of diluted CO<sub>2</sub>: metal-node-dependent activity and selectivity, *Angew. Chem. Int. Ed.* 57 (2018) 16811–16815, <https://doi.org/10.1002/anie.201811545>.
- [7] Z.B. Fang, T.T. Liu, J. Liu, S. Jin, X.P. Wu, X.Q. Gong, K. Wang, Q. Yin, T.F. Liu, R. Cao, H.C. Zhou, Boosting interfacial charge-transfer kinetics for efficient overall CO<sub>2</sub> photoreduction via rational design of coordination spheres on metal-organic frameworks, *J. Am. Chem. Soc.* 142 (2020) 12515–12523, <https://doi.org/10.1021/jacs.0c05530>.
- [8] N. Li, J. Liu, J.J. Liu, L.Z. Dong, Z.F. Xin, Y.L. Teng, Y.Q. Lan, Adenine components in biomimetic metal-organic frameworks for efficient CO<sub>2</sub> photoconversion, *Angew. Chem. Int. Ed.* 58 (2019) 5226–5231, <https://doi.org/10.1002/anie.201814729>.
- [9] S.L. Chan, T.L. Lam, C. Yang, S.C. Yan, N.M. Cheng, A robust and efficient cobalt molecular catalyst for CO<sub>2</sub> reduction, *Chem. Commun.* 51 (2015) 7799–7801, <https://doi.org/10.1039/c5cc00566c>.
- [10] L. Chen, Z. Guo, X.G. Wei, C. Gallenkamp, J. Bonin, E. Anxolabehere-Mallart, K. C. Lau, T.C. Lau, M. Robert, Molecular catalysis of the electrochemical and photochemical reduction of CO<sub>2</sub> with earth-abundant metal complexes. Selective



- production of CO vs HCOOH by switching of the metal center, *J. Am. Chem. Soc.* 137 (2015) 10918–10921, <https://doi.org/10.1021/jacs.5b06535>.
- [11] J. Bonin, M. Robert, M. Routier, Selective and efficient photocatalytic CO<sub>2</sub> reduction to CO using visible light and an iron-based homogeneous catalyst, *J. Am. Chem. Soc.* 136 (2014) 16768–16771, <https://doi.org/10.1021/ja510290t>.
  - [12] H. Takeda, K. Ohashi, A. Sekine, O. Ishitani, Photocatalytic CO<sub>2</sub> reduction using Cu (I) photosensitizers with a Fe(II) catalyst, *J. Am. Chem. Soc.* 138 (2016) 4354–4357, <https://doi.org/10.1021/jacs.6b01970>.
  - [13] V.S. Thoi, N. Kornienko, C.G. Margarit, P. Yang, C.J. Chang, Visible-light photoredox catalysis: selective reduction of carbon dioxide to carbon monoxide by a nickel N-heterocyclic carbene-isoquinoline complex, *J. Am. Chem. Soc.* 135 (2013) 14413–14424, <https://doi.org/10.1021/ja4074003>.
  - [14] H.X. Zhang, Q.L. Hong, J. Li, F. Wang, X.S. Huang, S.M. Chen, W.G. Tu, D.S. Yu, R. Xu, T.H. Zhou, J. Zhang, Isolated square-planar copper center in boron imidazolate nanocages for photocatalytic reduction of CO<sub>2</sub> to CO, *Angew. Chem. Int. Ed.* 131 (2019) 11878–11882, <https://doi.org/10.1002/anie.201905869>.
  - [15] P. Wang, R. Dong, S. Guo, J. Zhao, Z.M. Zhang, T.B. Lu, Improving photosensitization for photochemical CO<sub>2</sub>-to-CO conversion, *Nat. Sci. Rev.* 7 (2020) 1459–1467, <https://doi.org/10.1093/nsr/nwaa112/5848166>.
  - [16] A. Hossain, A. Bhattacharyya, O. Reiser, Copper's rapid ascent in visible-light photoredox catalysis, *Science* 364 (2019), eaav9713, <https://doi.org/10.1126/science.aav9713>.
  - [17] H. Shirley, X. Su, H. Sanjanwala, K. Talukdar, J.W. Jurss, J.H. Delcamp, Durable solar-powered systems with Ni-catalysts for conversion of CO<sub>2</sub> or CO to CH<sub>4</sub>, *J. Am. Chem. Soc.* 141 (2019) 6617–6622, <https://doi.org/10.1021/jacs.9b00937>.
  - [18] S. Fernandez, F. Franco, C. Casadevall, V. Martin-Diaconescu, J.M. Luis, J. Lloret-Fillol, A unified electro- and photocatalytic CO<sub>2</sub> to CO reduction mechanism with aminopyridine cobalt complexes, *J. Am. Chem. Soc.* 142 (2020) 120–133, <https://doi.org/10.1021/jacs.9b06633>.
  - [19] T. Ouyang, H.H. Huang, J.W. Wang, D.C. Zhong, T.B. Lu, A dinuclear cobalt cryptate as a homogeneous photocatalyst for highly selective and efficient visible-light driven CO<sub>2</sub> reduction to CO in CH<sub>3</sub>CN/H<sub>2</sub>O solution, *Angew. Chem. Int. Ed.* 56 (2017) 738–743, <https://doi.org/10.1002/anie.201610607>.
  - [20] T. Ouyang, H.J. Wang, H.H. Huang, J.W. Wang, S. Guo, W.J. Liu, D.C. Zhong, T. B. Lu, Dinuclear metal synergistic catalysis boosts photochemical CO<sub>2</sub>-to-CO conversion, *Angew. Chem. Int. Ed.* 57 (2018) 16480–16485, <https://doi.org/10.1002/anie.201811010>.
  - [21] D. Hong, T. Kawanishi, Y. Tsukakoshi, H. Kotani, T. Ishizuka, T. Kojima, Efficient photocatalytic CO<sub>2</sub> reduction by a Ni(II) complex having pyridine pendants through capturing a Mg<sup>2+</sup> ion as a Lewis-acid cocatalyst, *J. Am. Chem. Soc.* 141 (2019) 20309–20317, <https://doi.org/10.1021/jacs.9b10597>.
  - [22] E.A. Mohamed, Z.N. Zahran, Y. Naruta, Efficient electrocatalytic CO<sub>2</sub> reduction with a molecular cofacial iron porphyrin dimer, *Chem. Commun.* 51 (2015) 16900–16903, <https://doi.org/10.1039/C5CC04273A>.
  - [23] Z. Guo, G. Chen, C. Cometto, B. Ma, H. Zhao, T. Groizard, L. Chen, H. Fan, W. L. Man, S.M. Yiu, K.C. Lau, T.C. Lau, M. Robert, Selectivity control of CO versus HCOO<sup>-</sup> production in the visible-light-driven catalytic reduction of CO<sub>2</sub> with two cooperative metal sites, *Nat. Catal.* 2 (2019) 801–808, <https://doi.org/10.1038/s41929-019-0331-6>.
  - [24] J. Liu, Y.Z. Fan, X. Li, Z. Wei, Y.W. Xu, L. Zhang, C.Y. Su, A porous rhodium(III)-porphyrin metal-organic framework as an efficient and selective photocatalyst for CO<sub>2</sub> reduction, *Appl. Catal. B-Environ.* 231 (2018) 173–181, <https://doi.org/10.1016/j.apcatb.2018.02.055>.
  - [25] L.Y. Wu, Y.F. Mu, X.X. Guo, W. Zhang, Z.M. Zhang, M. Zhang, T.B. Lu, Encapsulating perovskite quantum dots in iron-based metal-organic frameworks (MOFs) for efficient photocatalytic CO<sub>2</sub> reduction, *Angew. Chem. Int. Ed.* 58 (2019) 9491–9495, <https://doi.org/10.1002/anie.201904537>.
  - [26] H.L. Nguyen, N. Hanikel, S.J. Lyle, C. Zhu, D.M. Proserpio, O.M. Yaghi, A porous covalent organic framework with voided square grid topology for atmospheric water harvesting, *J. Am. Chem. Soc.* 142 (2020) 2218–2221, <https://doi.org/10.1021/jacs.9b13094>.
  - [27] J.N. Lu, J. Liu, L.Z. Dong, S.L. Li, Y.H. Kan, Y.Q. Lan, Exploring the influence of halogen coordination effect of stable bimetallic MOFs on oxygen evolution reaction, *Chem. Eur. J.* 25 (2019) 15830–15836, <https://doi.org/10.1002/chem.201903482>.
  - [28] H.Q. Xu, J. Hu, D. Wang, Z. Li, Q. Zhang, Y. Luo, S.H. Yu, H.L. Jiang, Visible-light photoreduction of CO<sub>2</sub> in a metal-organic framework: boosting electron-hole separation via electron trap states, *J. Am. Chem. Soc.* 137 (2015) 13440–13443, <https://doi.org/10.1021/jacs.5b08773>.
  - [29] M. Elcheikh Mahmoud, H. Audi, A. Assoud, T.H. Ghaddar, M. Hmadeh, Metal-organic framework photocatalyst incorporating bis(4'-(4-carboxyphenyl)-terpyridine)ruthenium(II) for visible-light-driven carbon dioxide reduction, *J. Am. Chem. Soc.* 141 (2019) 7115–7121, <https://doi.org/10.1021/jacs.9b01920>.
  - [30] A. Zhou, Y. Dou, C. Zhao, J. Zhou, X.Q. Wu, J.R. Li, A leaf-branch TiO<sub>2</sub>/carbon@MOF composite for selective CO<sub>2</sub> photoreduction, *Appl. Catal. B-Environ.* 264 (2020), 118519, <https://doi.org/10.1016/j.apcatb.2019.118519>.
  - [31] Y. Dou, S.M. Xu, A. Zhou, H. Wang, J. Zhou, H. Yan, J.R. Li, Hierarchically structured semiconductor@noble-metal@MOF for high-performance selective photocatalytic CO<sub>2</sub> reduction, *GreenChE* 1 (2020) 48–55, <https://doi.org/10.1016/j.gce.2020.09.009>.
  - [32] Y. Chen, D. Wang, X. Deng, Z.H. Li, Metal-organic frameworks (MOFs) for photocatalytic CO<sub>2</sub> reduction, *Catal. Sci. Technol.* 7 (2017) 4893–4904, <https://doi.org/10.1039/C7CY01653K>.
  - [33] Y. Wang, N.Y. Huang, J.Q. Shen, P.Q. Liao, X.M. Chen, J.P. Zhang, Hydroxide ligands cooperate with catalytic centers in metal-organic frameworks for efficient photocatalytic CO<sub>2</sub> reduction, *J. Am. Chem. Soc.* 140 (2018) 38–41, <https://doi.org/10.1021/jacs.7b10107>.
  - [34] Z.H. Yan, M.H. Du, J. Liu, S. Jin, C. Wang, G.L. Zhuang, X.J. Kong, L.S. Long, L. S. Zheng, Photo-generated dinuclear [Eu(II)]<sub>2</sub> active sites for selective CO<sub>2</sub> reduction in a photosensitizing metal-organic framework, *Nat. Commun.* 9 (2018) 3353, <https://doi.org/10.1038/s41467-018-05659-7>.
  - [35] M.A. Nasalevich, C.H. Hendon, J.G. Santaclara, K. Svane, B. van der Linden, S. L. Veber, M.V. Fedin, A.J. Houtepen, M.A. van der Veen, F. Kapteijn, A. Walsh, J. Gascon, Electronic origins of photocatalytic activity in d0 metal organic frameworks, *Sci. Rep.* 6 (2016), 23676, <https://doi.org/10.1038/srep23676>.
  - [36] B. An, Z. Li, Y. Song, J. Zhang, L. Zeng, C. Wang, W.B. Lin, Cooperative copper centres in a metal-organic framework for selective conversion of CO<sub>2</sub> to ethanol, *Nat. Catal.* 2 (2019) 709–717, <https://doi.org/10.1038/s41929-019-0308-5>.
  - [37] M. Wang, D. Wang, Z. Li, Self-assembly of CPO-27-Mg/TiO<sub>2</sub> nanocomposite with enhanced performance for photocatalytic CO<sub>2</sub> reduction, *Appl. Catal. B-Environ.* 183 (2016) 47–52, <https://doi.org/10.1016/j.apcatb.2015.10.037>.
  - [38] C. Xu, Y. Pan, G. Wan, H. Liu, L. Wang, H. Zhou, S.H. Yu, H.L. Jiang, Turning on visible-light photocatalytic C-H oxidation over metal-organic frameworks by introducing metal-to-cluster charge transfer, *J. Am. Chem. Soc.* 141 (2019) 19110–19117, <https://doi.org/10.1021/jacs.9b09954>.
  - [39] X. Qiu, J. Chen, X. Zou, R. Fang, L. Chen, Z. Chen, K. Shen, Y.W. Li, Encapsulation of C-N-decorated metal sub-nanoclusters/single atoms into a metal-organic framework for highly efficient catalysis, *Chem. Sci.* 9 (2018) 8962–8968, <https://doi.org/10.1039/C8SC03549K>.
  - [40] Q. Huang, J. Liu, L. Feng, Q. Wang, W. Guan, L.Z. Dong, L. Zhang, L.K. Yan, Y. Q. Lan, H.C. Zhou, Multielectron transportation of polyoxometalate-grafted metalloporphyrin coordination frameworks for selective CO<sub>2</sub>-to-CH<sub>4</sub> photoconversion, *Nat. Sci. Rev.* 7 (2019) 53–63, <https://doi.org/10.1093/nsr/nwz096>.
  - [41] L. Shi, T. Wang, H. Zhang, K. Chang, X. Meng, H. Liu, J.H. Ye, An amine-functionalized iron(III) metal-organic framework as efficient visible-light photocatalyst for Cr(VI) reduction, *Adv. Sci.* 2 (2015), 1500006, <https://doi.org/10.1002/adv.201500006>.
  - [42] Y.S. Wei, M. Zhang, P.Q. Liao, R.B. Lin, T.Y. Li, G. Shao, J.P. Zhang, X.M. Chen, Coordination templated [2+2+2] cyclotrimerization in a porous coordination framework, *Nat. Commun.* 6 (2015) 8348, <https://doi.org/10.1038/ncomms9348>.
  - [43] Y. Song, Z. Li, Y. Zhu, X. Feng, J.S. Chen, M. Kaufmann, C. Wang, W.B. Lin, Titanium hydroxide secondary building units in metal-organic frameworks catalyze hydrogen evolution under visible light, *J. Am. Chem. Soc.* 141 (2019) 12219–12223, <https://doi.org/10.1021/jacs.9b05964>.
  - [44] P. Wang, S. Guo, H.J. Wang, K.K. Chen, N. Zhang, Z.M. Zhang, T.B. Lu, A broadband and strong visible-light-absorbing photosensitizer boosts hydrogen evolution, *Nat. Commun.* 10 (2019) 3155, <https://doi.org/10.1038/s41467-019-11099-8>.
  - [45] S. Guo, K.K. Chen, R. Dong, Z.M. Zhang, J. Zhao, T.B. Lu, Robust and long-lived excited state Ru(II) polyimine photosensitizers boost hydrogen production, *ACS Catal.* 8 (2018) 8659–8670, <https://doi.org/10.1021/acscatal.8b02226>.
  - [46] K.K. Chen, S. Guo, H. Liu, X. Li, Z.M. Zhang, T.B. Lu, Strong visible-light-absorbing cuprous sensitizers for dramatically boosting photocatalysis, *Angew. Chem. Int. Ed.* 59 (2020) 12951–12957, <https://doi.org/10.1002/anie.202003251>.
  - [47] D. Wang, R. Huang, W. Liu, D. Sun, Z. Li, Fe-based MOFs for photocatalytic CO<sub>2</sub> reduction: role of coordination unsaturated sites and dual excitation pathways, *ACS Catal.* 4 (2014) 4254–4260, <https://doi.org/10.1021/cs501169t>.